



# CHORUS

This is the accepted manuscript made available via CHORUS. The article has been published as:

## Hydrodynamic interactions in freely suspended liquid crystal films

Tatiana Kuriabova, Thomas R. Powers, Zhiyuan Qi, Aaron Goldfain, Cheol Soo Park, Matthew A. Glaser, Joseph E. Maclennan, and Noel A. Clark

Phys. Rev. E **94**, 052701 — Published 3 November 2016

DOI: [10.1103/PhysRevE.94.052701](https://doi.org/10.1103/PhysRevE.94.052701)

# Hydrodynamic Interactions in Freely Suspended Liquid Crystal Films

Tatiana Kuriabova

*Department of Physics, California Polytechnic State University, San Luis Obispo, California, 93407, USA*

Thomas R. Powers

*School of Engineering and Department of Physics,  
Brown University, Providence, Rhode Island, 02912, USA*

Zhiyuan Qi, Aaron Goldfain, Cheol Soo Park, Matthew A. Glaser, Joseph E. MacLennan, and Noel A. Clark

*Department of Physics and Soft Materials Research Center,  
University of Colorado, Boulder, Colorado, 80309, USA*

(Dated: October 9, 2016)

Hydrodynamic interactions play an important role in biological processes in cellular membranes, a large separation of length scales often allowing such membranes to be treated as continuous, two-dimensional (2D) fluids. We study experimentally and theoretically the hydrodynamic interaction of pairs of inclusions in two-dimensional, fluid smectic liquid crystal films suspended in air. Such smectic membranes are ideal systems for performing controlled experiments as they are mechanically stable, of highly uniform structure, and have well-defined, variable thickness, enabling experimental investigation of the crossover from 2D to 3D hydrodynamics. Our theoretical model generalizes the Levine/MacKintosh theory of point-force response functions and uses a boundary-element approach to calculate the mobility matrix for inclusions of finite extent. We describe in detail the theoretical and computational approach previously outlined in *Phys. Rev. Lett.* **113**, 128304 (2014) and extend the method to study the mutual mobilities of inclusions with asymmetric shapes. The model predicts well the observed mutual mobilities of pairs of circular inclusions in films and the self-mobility of a circular inclusion in the vicinity of a linear boundary.

PACS numbers: 47.57.Lj, 83.80.Xz, 68.15.+e, 83.60.Bc

## I. INTRODUCTION

Diffusion, aggregation and the long-range hydrodynamic interaction of proteins are common in many processes in fluid plasma membranes and the membranes of organelles. These proteins are usually much larger than the lipids that make up the membrane and the essential features of their dynamics can be captured by treating the membrane as a continuous, two-dimensional fluid. Since the membrane is typically embedded in some bulk fluid, with different viscosity, the motion of inclusions in the membrane generates flow not only in the membrane but in the surrounding fluid. Due to the momentum exchange between the membrane and the embedding fluid, the dynamics of the membrane displays features of both three-dimensional (3D) and two-dimensional (2D) hydrodynamics, behavior that has been dubbed “quasi-2D” hydrodynamics [1].

An accurate theoretical description of the hydrodynamics of membranes is essential for understanding their diffusive transport properties. Quasi-2D hydrodynamics is fundamentally different from 3D hydrodynamics, with the flow characterized by a characteristic length given by the ratio of the 2D membrane viscosity to the viscosity of the bulk fluid surrounding the membrane. This distance, known as the Saffman length [2–4], governs whether energy is dissipated primarily in the membrane or in the bulk and determines the spatial decay rate of the flow field in the membrane due to a perturbation.

As with passive microrheology in 3D, the Brownian motion of proteins and other inclusions in lipid membranes can serve as a direct probe of such membrane material properties as the viscosity. The translational diffusion coefficient  $D$  of an inclusion is related to its mobility  $\mu$  by the Einstein relation  $D = \mu k_B T$ , where  $k_B$  is the Boltzmann constant and  $T$  the temperature. Within the linear response regime of the fluid to an external force  $F$  (at low Reynolds number), the particle mobility is related to the particle velocity  $V$  by  $\mu = V/F$ . Analytical solutions for the mobility of an inclusion in 3D and 2D fluids have been found only in a limited number of cases. In 1975, Saffman and Delbrück (SD) proposed ways to avoid the so-called Stokes paradox, concerning the infinite mobility of a particle embedded in an unbounded 2D fluid in vacuum. SD showed that even in the case of a membrane in an embedding bulk fluid (such as air) with a viscosity much smaller than that of the membrane, the momentum exchange between the membrane and the surrounding fluid leads to a length scale that cuts off the logarithmically diverging mobility, thus avoiding the Stokes paradox [2].

Saffman went on to describe in detail the hydrodynamic problem of a disk of radius  $a$  moving with constant velocity in the plane of a 2D membrane of thickness  $h$  and viscosity  $\eta$  embedded in another viscous fluid of viscosity  $\eta'$  [3]. Saffman modeled the membrane as an incompressible fluid with uniform flow throughout the thickness of the membrane and a 2D viscosity  $\eta h$ . The presence of the bulk fluid allows the introduction of a useful length scale,

the so-called Saffman length,  $\ell_S = \eta h / (2\eta')$ , a characteristic hydrodynamic distance within which the membrane around the inclusion does not exchange momentum with the embedding fluid [3, 5].

By applying the incompressible Stokes equations to the bulk fluid and the membrane, and assuming no-slip boundary conditions, Saffman arrived at a set of integral equations describing the flow fields in the membrane. Obtaining an analytical solution for an arbitrary ratio of disk radius to the Saffman length,  $a/\ell_S$ , turned out to be very difficult. Saffman applied a singular perturbation technique to the particular case of a small inclusion in a thick membrane, where  $a\eta'/(h\eta) = a/\ell_S \ll 1$ . In this limit, the mobility of the inclusion depends only weakly (logarithmically) on its size:

$$\mu = \frac{1}{4\pi\eta h} \left[ \ln \left( \frac{2\ell_S}{a} \right) - \gamma \right], \quad (1)$$

where  $\gamma = 0.58$  is the Euler constant. This is in contrast to an unbounded 3D fluid, where the mobility of a sphere is inversely proportional to its radius. By solving the Stokes equations numerically, Heringa, Wiegel, and van Beckum [6, 7] computed the mobility of cylindrical inclusions of arbitrary size in embedded membranes, obtaining results that are in good agreement with a more general, analytical model developed subsequently by Hughes, Pailthorpe, and White (HPW) [4], who heroically solved Saffman's integral equations for arbitrary  $a/\ell_S$  ratios. Their full solution for the disk mobility shows a crossover from the 2D logarithmic behavior of Eq. (1) for small  $a/\ell_S$  to a 3D-like dependence  $\mu \propto 1/a$  when  $a/\ell_S \gg 1$ . Petrov and Schwille subsequently derived an accurate approximation to the complicated HPW mobility expression [8].

Aspects of the SD/HPW predictions for single inclusion have been verified experimentally [9–11]. The dependence of mobility on inclusion size, and its crossover from three-dimensional to two-dimensional behavior as inclusion size decreases, have recently been confirmed in experiments on thin smectic liquid crystal films [12].

There has, however, been comparatively little work on the hydrodynamic interactions between multiple inclusions in thin fluid films. When there is more than one inclusion in the membrane, as is typical in biological systems, their mobilities depend not only on their size and the drag from the surrounding fluid but also on hydrodynamic interactions between the inclusions. Hammer and collaborators [13] calculated the mobilities of two cylinders in a membrane in the limit  $a \ll \ell_S$ . In the extreme case of a pair of inclusions with one inclusion being much larger than the other, the problem reduces to evaluating the hydrodynamic interaction of a particle with a stationary or mobile geometric boundary.

Levine and MacKintosh (LM), in work prompted by microrheology experiments on quasi-2D viscoelastic membranes, derived the response tensor  $\alpha_{\alpha\beta}(\mathbf{x} - \mathbf{x}')$  that determines the local displacement of the membrane at position  $\mathbf{x}'$  due to an in-plane, localized force  $\mathbf{f}(\mathbf{x}) =$

$\mathbf{f}\delta(\mathbf{x})$  [14]. In the case of a purely viscous membrane, there is no elastic deformation of the membrane, and its physical properties can be described by the velocity field alone, given by

$$v_\alpha(\mathbf{x}) = \alpha_{\alpha\beta}(\mathbf{x} - \mathbf{x}') f_\beta(\mathbf{x}'). \quad (2)$$

Here a summation is carried out over repeated indexes and  $\alpha, \beta = x, y$ . In our notation,  $\alpha_{\alpha\beta}$  corresponds to  $-i\omega\alpha_{\alpha\beta}$  in the LM theory. The response function  $\alpha_{\alpha\beta}$  in Eq. (2) plays the role of the Oseen tensor in 3D hydrodynamics.

When the separation between two membrane inclusions is much greater than their sizes, the inclusions may be modeled as points on the membrane. In this limit, the response function  $\alpha_{\alpha\beta}$  corresponds to the far-field approximation of hydrodynamic coupling between the inclusions, the so-called mutual mobility.

As was shown by LM, the response function may be split into ‘parallel’ and ‘transverse’ contributions:

$$\alpha_{\alpha\beta}(\mathbf{x}) = \alpha_{\parallel}(|\mathbf{x}|)\hat{x}_\alpha\hat{x}_\beta + \alpha_{\perp}(|\mathbf{x}|)[\delta_{\alpha\beta} - \hat{x}_\alpha\hat{x}_\beta]. \quad (3)$$

The scalar functions  $\alpha_{\parallel}$  and  $\alpha_{\perp}$  are given by

$$\alpha_{\parallel}(z) = \frac{1}{4\pi\eta h} \left[ \frac{\pi}{z} \mathbf{H}_1(z) - \frac{2}{z^2} - \frac{\pi}{2} [Y_0(z) + Y_2(z)] \right] \quad (4)$$

$$\alpha_{\perp}(z) = \frac{1}{4\pi\eta h} \left[ \pi \mathbf{H}_0(z) - \frac{\pi}{z} \mathbf{H}_1(z) + \frac{2}{z^2} - \frac{\pi}{2} [Y_0(z) - Y_2(z)] \right], \quad (5)$$

where  $\mathbf{H}_\nu$  are Struve functions and  $Y_\nu$  are Bessel functions of the second kind [15];  $z = |\mathbf{x}|/\ell_S$  is the non-dimensionalized distance between the point of application of the force and the point where the membrane velocity response is measured. Both  $\alpha_{\parallel}(z)$  and  $\alpha_{\perp}(z)$  diverge logarithmically as  $z \rightarrow 0$ , while for large  $z$  we have  $\alpha_{\parallel}(z) \sim 1/z$  and  $\alpha_{\perp}(z) \sim 1/z^2$ .

Here,  $\alpha_{\parallel}$  ( $\alpha_{\perp}$ ) corresponds to the far-field approximation of the mutual mobility of two inclusions when they move parallel (perpendicular) to the line connecting their centers. The expressions for the far-field mutual mobilities in Eqs. (4) and (5) have no dependence on the inclusion size  $a$ . Oppenheimer and Diamant found an analytical correction of the order  $(a/r)^2$  to the far-field mobilities  $\alpha_{\parallel}$  and  $\alpha_{\perp}$ , where  $a$  is the size of the inclusions and  $r$  is the distance between the inclusion centers [1]. They also showed that finite-size effects set in for distances  $r \leq (a^2\ell_S)^{1/3}$ . We have developed an extension of the LM model and a computational approach for modeling the hydrodynamic interactions of pairs of oil drops and thickness “islands” in smectic liquid crystal films and have tested our predictions against experimental measurements [16]. Noruzifar *et al.* [17] have also recently described a computational regularized Stokeslets method that confirms the analytical results of Oppenheimer and

Diamant, is applicable to a broad range of parameters, and can be generalized to many-body systems.

Many biological inclusions such as proteins and lipid rafts are not perfectly circular and their mobilities are expected to deviate from the idealized predictions of Saffman and HPW. The approaches developed in [16] and [17] both allow a straightforward extension to computing the hydrodynamic interaction of inclusions of arbitrary shape.

In biomembranes, it is difficult to measure viscosities and to vary the length scales  $a$  and  $\ell_S$  over a wide range. Smectic liquid crystals, on the other hand, in which rod-like molecules are arranged in stacks of liquid layers, are ideal experimental systems for studying hydrodynamics in 2D [18–20]. Ultra-thin, freely suspended smectic films have a highly uniform structure and well-defined thickness. Compared with soap films, smectic films are much more stable against being distorted or ruptured, and less sensitive to changes in temperature and humidity. Smectic films can be made as thin as a few molecular layers and are stable for hours and days [12, 16, 21]. Furthermore, in many fluid smectics, all of the hydrodynamically relevant physical parameters have been measured.

In this paper, we describe in detail the theoretical and computational approach for calculating the mutual mobilities of inclusions in thin fluid membranes previously outlined in [16] and compare the results with experiment. We also report calculations of the mobility of a circular inclusion in the vicinity of a linear boundary, motivated by our recent experiments. A multipole expansion approach allows us to understand a peculiar characteristic of the observed radial mutual mobility of two identical, circular inclusions. We also discuss the hydrodynamic interactions of two elliptical inclusions, and the effects of asymmetrical inclusion shapes on their mutual mobility.

This article is organized as follows: In Sec. II we discuss the effect of a nearby boundary on the mobility of a circular inclusion embedded in a quasi-2D membrane, considering a range of inclusion sizes, Saffman lengths, and separations between the inclusion and the boundary, and compare the theoretical predictions with experiment. In Sec. III we consider the hydrodynamic interactions of two identical, circular islands. In Sec. IV we develop a multipole expansion of the fluid velocity field around clusters of small, disk-like inclusions that move as rigid bodies within a quasi-2D membrane, and demonstrate the dominant role of the leading order term in the hydrodynamic interactions of such clusters that are geometrically symmetric. Finally, in Sec. V we discuss our results and suggest further avenues of investigation.

## II. MOBILITY OF AN INCLUSION NEAR A STRAIGHT BOUNDARY

In a three-dimensional fluid, the mobility of a sphere of radius  $a$  with its center a distance  $x$  from a wall such

that  $x \gg a$  is given by [22–24]

$$\frac{\mu_{\perp}}{\mu_0} \approx 1 - \frac{9}{8} \left(\frac{a}{x}\right) + \frac{1}{2} \left(\frac{a}{x}\right)^3 + O\left(\left(\frac{a}{x}\right)^4\right), \quad (6a)$$

$$\frac{\mu_{\parallel}}{\mu_0} \approx 1 - \frac{9}{16} \left(\frac{a}{x}\right) + O\left(\left(\frac{a}{x}\right)^3\right), \quad (6b)$$

where  $\mu_{\perp}$  and  $\mu_{\parallel}$  are the mobilities of the sphere for motion perpendicular and parallel to the wall and  $\mu_0$  is the mobility of the sphere in unbounded fluid.

We have investigated the analogous problem of a disk-like inclusion diffusing in a quasi-2D membrane in the vicinity of a linear boundary. In our experiments, we observed the Brownian motion of smectic islands embedded in square, freely suspended smectic films in the proximity of a meniscus. These islands are disk-shaped, thicker regions of the film bounded by edge dislocations, as indicated in Fig. 1. The islands were between a few and several hundred  $\mu\text{m}$  in radius  $a$ . The liquid crystal used in our experiments is 8CB (4'-n-octyl-4'-cyanobiphenyl, Sigma-Aldrich), a room-temperature smectic A material. The density and viscosity of 8CB are  $\rho \approx 0.96 \text{ g/cm}^3$  [25] and  $\eta = 0.052 \text{ Pa} \cdot \text{s}$  [26], respectively, while the viscosity of ambient air is  $\eta' = 1.827 \times 10^{-5} \text{ Pa} \cdot \text{s}$  [27]. Each smectic layer has a thickness of 3.17 nm [28].

Freely suspended films were created by spreading a small amount of the liquid crystal across a  $5 \text{ mm} \times 5 \text{ mm}$  hole in a glass cover slip. The films were typically from two to six molecular layers thick, corresponding to Saffman lengths between 9 and 27  $\mu\text{m}$ , and were observed using reflected light microscopy. Immediately after a film is drawn, there are typically many islands present, with a range of diameters. The film may then be gently sheared using an air jet to break larger islands into smaller ones for study. The films are carefully leveled to minimize gravitational drift, allowing us to record the motion of the islands, with high spatial resolution at a typical video frame rate of 24 fps. In these experiments, isolated islands far from other inclusions but in the proximity of the meniscus along one of the film boundaries were selected for study.

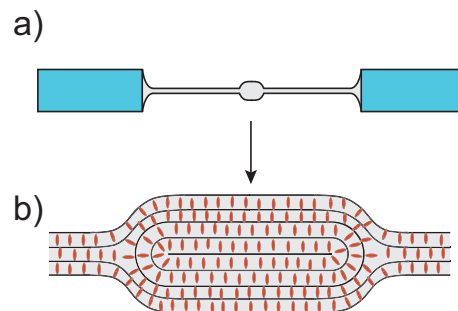


FIG. 1. Color online. Schematic illustration of a) a smectic A film suspended across an aperture and b) the cross-section of a circular island, eight molecular layers thick, embedded in a three-layer film.

The motion of inclusions in smectic films is thermally

driven and occurs in the low Reynolds number regime ( $Re = \rho va/\eta \ll 1$  and  $Re' = \rho' va/\eta' \ll 1$ ). In this limit, we have creeping flow, where viscous forces dominate, inertial effects are negligible, and the Stokes equations apply.

Suppose a mobile inclusion is subjected to an external force  $\mathbf{F}$  applied in the plane of the membrane. The linearity of the Stokes equations implies that the resultant velocity of the inclusion is a linear function of the force,

$$\mathbf{V} = \mathbf{M}\mathbf{F}, \quad (7)$$

where  $\mathbf{M}$ , the mobility tensor, depends on the shape of the inclusion and the boundary conditions. For simplicity we model the meniscus as an infinite linear boundary that lies in the plane of the membrane.

When the distance between the inclusion and the boundary is much greater than the inclusion radius, it is reasonable to apply a simplified method of reflections, similar to the 3D version described by Happel and Brenner [29]. We approximate the flow field due to a moving circular inclusion by the flow field due to a single force applied to the membrane at the inclusion center. We introduce a continuous distribution of ‘image’ forces along the boundary and impose a no-slip boundary condition at the stationary boundary. A coordinate system is chosen with an origin in the center of the inclusion, and the linear boundary is located at  $x = d$  (see Fig. 2). Let us suppose that the inclusion moves with velocity  $\mathbf{V} = V\hat{x}$  perpendicular to the boundary. In the zeroth approximation (in the absence of a boundary), the viscous drag force on the inclusion is given by the known HPW relation  $\mathbf{F}^{(0)} = -V\hat{x}/\mu_0(a)$ , where  $\mu_0(a)$  is the mobility of a disk of radius  $a$  in unbounded membrane [4].

The magnitudes and orientations of the image forces at the boundary must be adjusted to ‘cancel’ the flow field due to the moving island and preserve the no-slip boundary condition at the boundary. The image forces, in turn, generate a ‘reflected’ flow field in the membrane. We denote the ‘reflected’ fluid velocity at the island center as  $\mathbf{v}_r^{(1)}$ . Due to the linearity of the Stokes equations and the  $y \rightarrow -y$  symmetry, this fluid velocity is proportional to  $\mathbf{F}^{(0)}$ , and we may write  $\mathbf{v}_r^{(1)} \equiv -\gamma(d)\mathbf{F}^{(0)}$ , where  $\gamma(d)$  is an initially unknown coefficient of proportionality that depends on the distance  $d$  to the boundary. The first correction to the viscous drag force on the inclusion is given by

$$\mathbf{F}^{(1)} = -\frac{\mathbf{v}_r^{(1)}}{\mu_0(a)} = \frac{\gamma(d)\mathbf{F}^{(0)}}{\mu_0(a)} = -\frac{\gamma(d)}{(\mu_0(a))^2}V\hat{x}. \quad (8)$$

Therefore, the inclusion exerts an additional force  $-\mathbf{F}^{(1)}$  on the membrane. By assumption, this force is localized at the inclusion center. In the next order of the method of reflections, the velocity field ‘reflected’ from the boundary gives the fluid velocity  $\mathbf{v}_r^{(2)} = -\gamma(d)\mathbf{F}^{(1)}$  at the inclusion center, and the next correction to the drag force on the inclusion becomes

$$\mathbf{F}^{(2)} = -\frac{\mathbf{v}_r^{(2)}}{\mu_0(a)} = \frac{\gamma(d)\mathbf{F}^{(1)}}{\mu_0(a)} = -\frac{1}{\mu_0(a)} \left[ \frac{\gamma(d)}{\mu_0(a)} \right]^2 V\hat{x}. \quad (9)$$

Continuing this process we find that the total viscous drag force on the inclusion is given by

$$\begin{aligned} \mathbf{F} &= \mathbf{F}^{(0)} + \mathbf{F}^{(1)} + \mathbf{F}^{(2)} + \dots \\ &= -\frac{V}{\mu_0(a)} \left( 1 + \frac{\gamma(d)}{\mu_0(a)} + \left[ \frac{\gamma(d)}{\mu_0(a)} \right]^2 + \dots \right) \hat{x} \\ &= -\frac{V}{\mu_0(a)(1 - \gamma(d)/\mu_0(a))} \hat{x}. \end{aligned} \quad (10)$$

We can define the ‘renormalized’ mobility of an inclusion due to the presence of a boundary as

$$\mu_{\perp}(a, d) = \mu_0(a) \left( 1 - \gamma(d)/\mu_0(a) \right). \quad (11)$$

A similar equation may be derived for  $\mu_{\parallel}(a, d)$ , the mobility of an inclusion moving parallel to the boundary. We describe the computation of the reflected velocity field and the parameter  $\gamma(d)$  in Eq. (11) in more detail in Appendix A.

The approximate method of reflections that we have just outlined is relatively simple but it does not allow us to assess the accuracy of its predictions. To test the range of applicability of the far-field approximation, we developed a more rigorous approach to computing the renormalized mobilities  $\mu_{\perp}$  and  $\mu_{\parallel}$  that we call the boundary-element method (BEM). In this expanded computational approach, we assume that the velocity field due to an inclusion can be modeled as the velocity field due to a continuous distribution of (initially unknown) force densities applied to the membrane along the inclusion circumference and the stationary boundary (see Fig. 2). The linearity of the Stokes equations dictates that the net flow field is a superposition of the flow fields generated by all of the forces applied to the membrane. The force densities are determined by the boundary conditions on the fluid velocity. This is an extension of the technique introduced by LM to compute the mobility of an infinitesimally thin, cylindrical inclusion embedded in a quasi-2D membrane [30].

The flow field at point  $\mathbf{x}'$  in the membrane due to the motion of the inclusion is found by superposing the effects of the localized forces distributed both on the inclusion circumference and along the film boundary:

$$\begin{aligned} v^{\alpha}(\mathbf{x}') &= \int_0^{2\pi} f^{\beta}(\phi) \alpha_{\alpha\beta}(\mathbf{x}' - \mathbf{x}(\phi)) d\phi \\ &+ \int_{-\infty}^{\infty} g^{\beta}(y) \alpha_{\alpha\beta}(\mathbf{x}' - \mathbf{x}(y)) dy, \end{aligned} \quad (12)$$

where  $\alpha, \beta = x, y$ ,  $\mathbf{x}(\phi) = a \cos \phi \hat{x} + a \sin \phi \hat{y}$  and  $\mathbf{x}(y) = d\hat{x} + y\hat{y}$  describe respectively the loci of the inclusion and film boundaries,  $f^{\beta}(\phi)$  and  $g^{\beta}(y)$  are the (initially unknown) strengths of the point forces on these

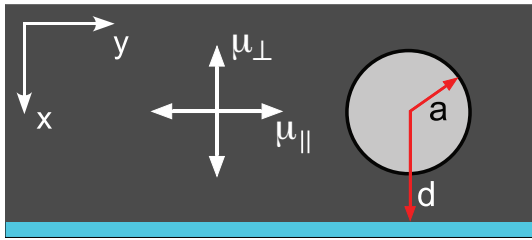


FIG. 2. Cartoon of a circular smectic island in the vicinity of a linear boundary (top view). In the far-field limit, the flow field due to the island may be approximated as the flow field due to a single force applied at the center of the island. In the BEM computations, we consider continuous distributions of forces along both the inclusion’s circumference and along the linear boundary.

boundaries, and  $\alpha_{\alpha\beta}$  is the LM response function shown in Eq. (3).

The smectic islands observed in our experiments do have fluid interiors. However, the permeative flow across the island boundaries and circulatory flow inside the islands induced by their Brownian motion through the background film are expected to be strongly suppressed, so that they behave hydrodynamically like solid discs. The permeative flow in smectics well below the nematic–smectic A phase transition is very slow [31, 32]. Indeed, on the time scale of our experiments, the island radii (typically tens to hundreds of  $\mu\text{m}$ ) are essentially constant, changing only very slowly with time. Since the islands have more smectic layers than the surrounding film, they are intrinsically much more viscous, and the flow within the islands can be neglected. We, therefore, assume that the islands move as rigid bodies and that every point of an island moves with the same velocity  $\mathbf{V}$ .

Strictly speaking, a rigid inclusion should be modeled by a continuous distribution of forces over the entire inclusion area, not only by those on its rim. However, even when the forces are applied only at the inclusion’s circumference, the computed fluid velocity field inside the rigid perimeter is found to be essentially uniform (see Fig. 3), and the calculated mobilities of isolated rigid rings with experimentally relevant radii ( $0.1\ell_S < a < 10\ell_S$ ) agree within 3% with the results of HPW for a rigid disk [4]. We therefore conclude that modeling the inclusion using only the forces on its circumference is sufficiently accurate for our purposes. Tiling the entire area of an inclusion with regularized Stokeslets may be necessary for modeling larger rigid inclusions [17, 33] but is computationally much more expensive.

The force densities  $f^\beta(\phi)$ ,  $g^\beta(y)$  in Eq. (12) are found by demanding the no-slip conditions  $v^\alpha = V^\alpha$ ,  $v^\alpha = 0$  on the circular and linear boundaries, respectively, and then numerically solving Eq. (12). The numerical procedure is outlined in Appendix A.

The viscous drag force on the inclusion is found by integrating the localized forces  $f^\beta(\phi)$  at the inclusion bound-

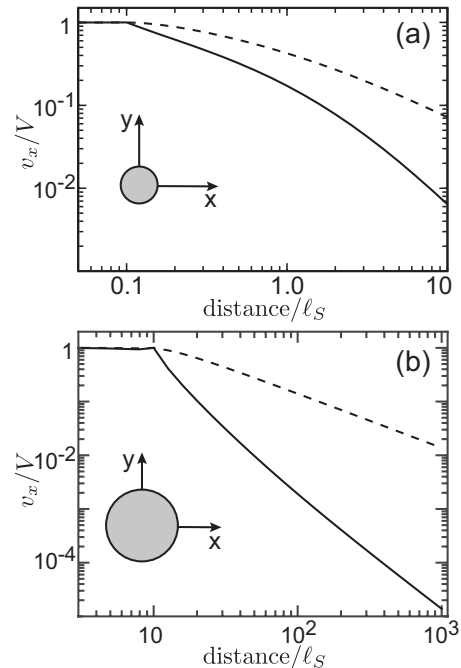


FIG. 3. Calculated  $x$ -component of the fluid velocity field  $v_x$  along the  $x$ -axis (dashed line) and along the  $y$ -axis (solid line) due to a single circular inclusion modeled as a rigid ring of radius (a)  $a = 0.1\ell_S$  and (b)  $a = 10\ell_S$  moving with velocity  $\mathbf{V}$  along the  $x$ -axis in a 2D unbounded membrane. Note that the computed velocity field inside the rigid ring is nearly uniform, validating our simplified modeling of a disk-like inclusion using point forces only on the inclusion boundary. For distances  $r < \ell_S$  from the center of the ring and comparable to the size of the inclusion,  $v_x$  falls off (a) logarithmically along both  $x$  and  $y$  in the case of small inclusions, (b) as  $1/r$  along  $x$  and as  $1/r^2$  along  $y$  when the inclusions are large.

ary:

$$F^\alpha = \int_0^{2\pi} f^\alpha(\phi) d\phi. \quad (13)$$

When the coupling between the translational and rotational motion of an island can be neglected (see Appendix A), it is sufficient to consider two special cases, with the inclusion moving either parallel or perpendicular to the boundary. In the case of parallel motion, the drag force has by symmetry only a  $y$ -component, and the velocity of the inclusion is directly proportional to the force:

$$V = \mu_{\parallel} F, \quad (14)$$

where  $\mu_{\parallel}$  denotes the inclusion mobility for motion parallel to boundary. In our numerical computations, we set the island velocity  $\mathbf{V}$  to a unit vector along  $\hat{y}$ . From Eq. (13), the mobility is then  $\mu_{\parallel} = [\int_0^{2\pi} f^y(\phi) d\phi]^{-1}$ . In the case of an inclusion moving perpendicular to the boundary, on the other hand, we have

$$V = \mu_{\perp} F, \quad (15)$$

where  $\mu_{\perp}$  is the inclusion mobility for perpendicular motion. With  $\mathbf{V}$  a unit vector along  $\hat{x}$ , we have  $\mu_{\perp} = [\int_0^{2\pi} f^x(\phi)d\phi]^{-1}$ .

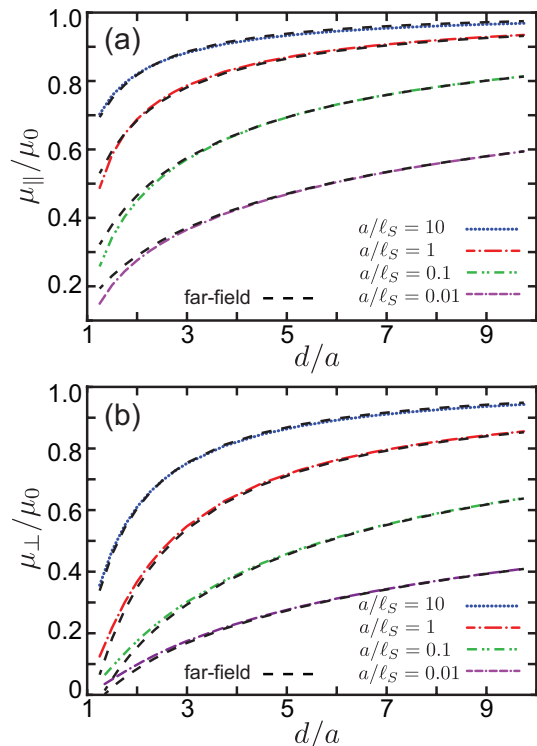


FIG. 4. Color online. Calculated mobility of a circular inclusion (scaled by the HPW mobility  $\mu_0$ ) moving a) parallel and b) perpendicular to a linear film boundary as a function of the distance  $d$  from the inclusion center to the boundary (scaled by the inclusion radius  $a$ ). The colored (gray) curves are the results of BEM computations, with the black dashed curves showing the far-field approximations.

The predictions of the LM far-field approximation and of the BEM calculations are compared in Fig. 4, where we plot the translational mobilities  $\mu_{\parallel}$  and  $\mu_{\perp}$  scaled by the HPW mobility  $\mu_0$  of a disk of radius  $a$  in an unbounded membrane vs. distance  $d$  to the boundary. Surprisingly, the far-field approximation reproduces the BEM computations down to distances to the boundary as small as two or three inclusion radii. For island radii  $a < \ell_S$ , where the energy dissipation occurs primarily in the membrane rather than in the bulk fluid, we observe a slower approach of  $\mu_{\parallel}$  and  $\mu_{\perp}$  to the HPW mobility  $\mu_0$  with increasing distance  $d$  from the boundary than in the case of inclusions with  $a > \ell_S$ . This is consistent with the slower (logarithmic) decay of the flow field characteristic of 2D hydrodynamics.

In the next section, we compare these predictions with experimental measurements.

## Comparison with experiment

We tracked the motion of inclusions in 8CB films at different distances from the film boundary using digital video microscopy, using Canny's method for edge detection [34] and Taubin's method [35] to find the positions and sizes of inclusions. We analytically removed the effect of residual drift [12] and computed the mean square displacements  $\langle \Delta \mathbf{r}^2(t) \rangle$ , where  $\Delta \mathbf{r}$  is the displacement of an island in time interval  $t$ . The inclusion mobility  $\mu$  was then determined using the Einstein relation:

$$\langle \Delta \mathbf{r}^2(t) \rangle = 4\mu k_B T t. \quad (16)$$

The experimentally measured mobilities  $\mu_{\parallel}$  and  $\mu_{\perp}$  (scaled by  $4\pi\eta h$ ) are shown, together with the theoretical predictions, in Fig. 5. We observe reasonably good correspondence between the predictions of our model and the experimental measurements, supporting the assumption that the long-range hydrodynamic interaction between the inclusion and the boundary dominates all other possible interactions, confirming that a no-slip boundary condition at the meniscus is justified [36].

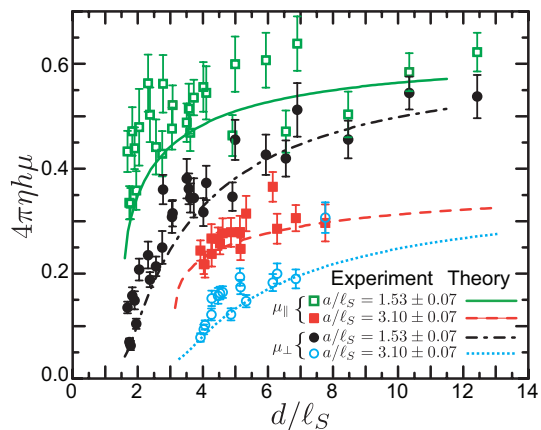


FIG. 5. Color online. Measured and predicted translational mobilities  $\mu_{\parallel}$  and  $\mu_{\perp}$  of islands of different sizes as a function of the dimensionless distance  $d/\ell_S$  to a linear boundary.

## III. THE MUTUAL MOBILITY OF TWO CIRCULAR INCLUSIONS

In this section we briefly review our recent experiments on Brownian motion of pairs of circular inclusions embedded in smectic A freely suspended films [16] and provide an expanded description of our theoretical and computational method for studying the hydrodynamic interaction of the inclusions.

In the experiments we recorded the Brownian motion of isolated pairs of smectic islands (with diameters of tens and hundreds of  $\mu\text{m}$ ) and smaller silicone oil droplets (with diameters of a few and tens of  $\mu\text{m}$ ) embedded in freely suspended films, shown in Fig. 6.

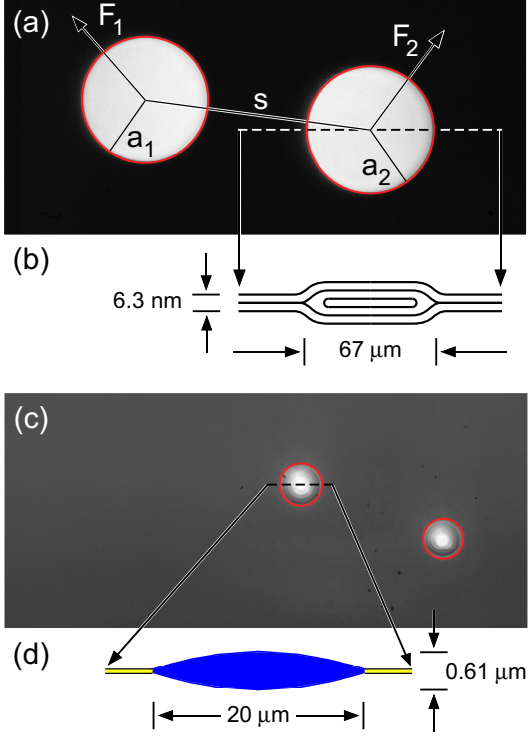


FIG. 6. Color online. Island and silicone oil droplet pairs in thin 8CB films viewed in reflection. (a) Islands with radii  $a_1$  and  $a_2$  and center-to-center separation  $s$  subject to the forces  $F_1$  and  $F_2$ . (b) Schematic cross section of a five-layer island in a two-layer film (the vertical dimension is greatly exaggerated for clarity). (c) Silicone oil droplets embedded in a six-layer film. (d) Cross-section of a typical silicone oil inclusion (drawn with expanded vertical scale), measured using optical interference in monochromatic light [37].

Using the approach discussed in the previous section, we computed the cross-correlation functions  $\langle \Delta \mathbf{r}_1(t) \cdot \Delta \mathbf{r}_2(t) \delta(r_{12}(0) - s) \rangle$ , where  $\Delta \mathbf{r}_k(t) = \mathbf{r}_k(t) - \mathbf{r}_k(0)$  are displacements of the  $k$ -th inclusion in time interval  $t$  and  $r_{12}(0)$  and  $s$  are respectively the distances between the centers of the inclusions at  $t = 0$  and at time  $t$  (see Fig. 6a). The cross-correlation functions contain information about long-range hydrodynamic interactions of the inclusions mediated by the smectic film and can be expressed in terms of the so-called mobility matrices.

If the inclusions are subjected to external forces  $\mathbf{F}_1$  and  $\mathbf{F}_2$ , respectively, the linearity of the Stokes equations dictates that the velocity of each inclusion is a linear function of all of the forces. For example, the velocity of inclusion ‘1’ is

$$\mathbf{V}_1 = \mathbf{M}_{11} \mathbf{F}_1 + \mathbf{M}_{12} \mathbf{F}_2, \quad (17)$$

where  $\mathbf{M}_{11}$  is the self-mobility matrix and  $\mathbf{M}_{12}$  the mutual mobility matrix.

For a pair of circular inclusions the only non-vanishing components of the mobility matrices are the diagonal elements  $M_{11}^{rr}$ ,  $M_{11}^{\theta\theta}$ ,  $M_{12}^{rr}$ , and  $M_{12}^{\theta\theta}$ , where  $rr$  refers to the

radial motion of the inclusions (along the line connecting their centers), and  $\theta\theta$  to tangential motion (perpendicular to this line). All other terms in the mobility matrices vanish due to the mirror symmetry about the line connecting the inclusion centers. The mutual mobilities can be extracted directly from the cross-correlation functions (see Appendix C):

$$\langle \Delta \mathbf{r}_1(t) \cdot \Delta \mathbf{r}_2(t) \delta(r_{12}(0) - s) \rangle = 2k_B T (M_{12}^{rr}(s) + M_{12}^{\theta\theta}(s)) t. \quad (18)$$

Similarly to our treatment of an inclusion in the vicinity of a boundary, we model the flow field in the membrane due to the moving inclusions by the flow field due to a continuous distribution of forces along the inclusions’ circular boundaries. The flow field at point  $\mathbf{x}'$  in the membrane is then given by

$$v^\alpha(\mathbf{x}') = \sum_{j=1,2} \int_0^{2\pi} f_j^\beta(\phi) \alpha_{\alpha\beta}(\mathbf{x}' - \mathbf{x}_j(\phi)) d\phi, \quad (19)$$

where  $\alpha, \beta = x, y$ ;  $j = 1, 2$  label the inclusion,  $f_j^\beta(\phi)$  are the strengths of the point forces, and the points  $\mathbf{x}_j(\phi)$  are along the circumference of the  $j$ th inclusion.

We apply the same arguments that we presented in the previous section, assuming no-slip boundary conditions for both smectic islands and oil drops. Silicone oil drop inclusions can be considered as solid-like because the tremendous increase of the areal viscosity in the boundary regions allows the velocity field of the film to penetrate only a very short distance into the thicker regions of these lens-shaped objects. As is the case with islands, experimental measurements confirm that the diffusion of oil droplets is also well described by SD-HPW theory, suggesting that any internal flow within the oil droplets can safely be ignored [36].

We find the force densities  $f_j^\beta(\phi)$  in Eq. (19), with the no-slip conditions  $v_j^\alpha = V_j^\alpha$  on both circular boundaries and then solve Eq. 19 numerically. These computations are described in more detail in Appendix B.

The viscous drag on the  $j$ th inclusion is given by the sum of the localized forces  $f_j^\alpha(\phi)$ :

$$F_j^\alpha = \int_0^{2\pi} f_j^\alpha(\phi) d\phi, \quad j = 1, 2. \quad (20)$$

By considering the four special inclusion configurations shown in Fig. 7, we computed the drag forces and determined the self- and mutual mobilities  $M_{11}^{rr}$ ,  $M_{11}^{\theta\theta}$ ,  $M_{12}^{rr}$ , and  $M_{12}^{\theta\theta}$ .

We have also computed the self-mobilities  $M_{11}^{rr}$  and  $M_{11}^{\theta\theta}$  of an inclusion in the presence of a neighbor. These are plotted in Fig. 8 as a function of the non-dimensionalized center-to-center distance  $s/\ell_S$  between the neighbors for inclusions of different sizes, scaled by the corresponding mobility of an isolated inclusion  $\mu_0$ . Both the translational and rotational self-mobilities are predicted by the model to be reduced when the inclusion is in close proximity to a neighbor but this effect is

relatively short-ranged and weak and has proven to be difficult to measure in our experiments.

The mutual mobilities  $M_{12}^{rr}$  and  $M_{12}^{\theta\theta}$  computed using the BEM model are shown in Fig. 9. In the following section, we compare these predictions with experiment.

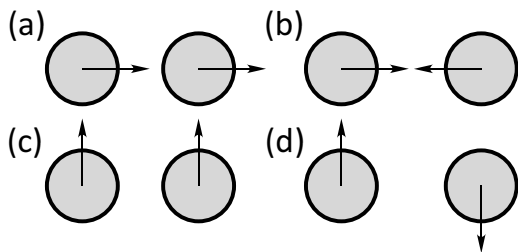


FIG. 7. Pairs of membrane inclusions moving in response to applied forces. The arrows represent simultaneously the forces applied to the inclusions (which all have the same magnitude) and the resultant velocities of the inclusion centers. The fluid at infinity is assumed to be at rest. Determination of the viscous drag force found by applying Eq. 17 to each case yields the following mobility combinations: (a)  $M_{11}^{rr} + M_{12}^{rr}$ , (b)  $M_{11}^{rr} - M_{12}^{rr}$ , (c)  $M_{11}^{\theta\theta} + M_{12}^{\theta\theta}$ , (d)  $M_{11}^{\theta\theta} - M_{12}^{\theta\theta}$ .

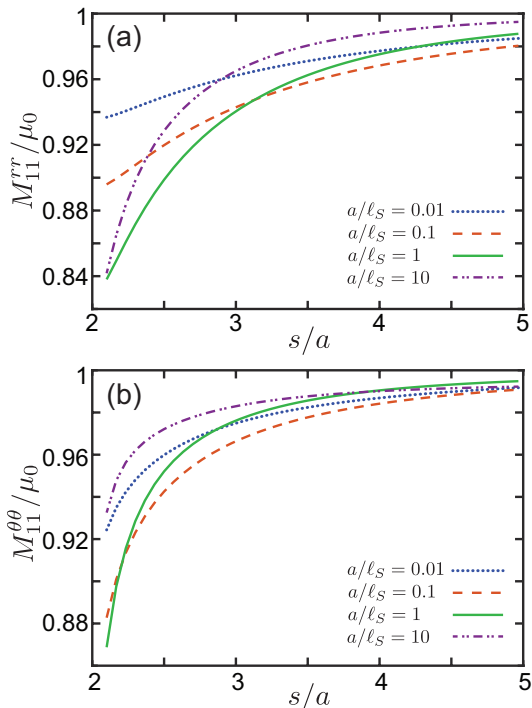


FIG. 8. Color online. Calculated self-mobilities scaled by the mobility of an isolated inclusion in an unbounded domain for inclusions moving a) along the line connecting their centers b) perpendicular to the line connecting their centers as a function of the non-dimensionalized center-to-center distance  $s/\ell_S$  between the inclusions for various inclusion radii scaled by the Saffman length.

## Comparison with experiment

When the centers of two inclusions in the film are separated by distances much larger than the inclusion radius, we observe, as expected, that their mutual mobilities  $M_{12}^{rr}$  and  $M_{12}^{\theta\theta}$  follow the far-field solutions given by the LM response functions  $\alpha_{\parallel}$  and  $\alpha_{\perp}$ , and the self-mobilities  $M_{11}$ ,  $M_{22}$  follow the HPW predictions for isolated inclusions. These experimental results are consistent with the observations of Prasad *et al.* [38], who studied the correlated motion of colloidal particles diffusing along an air-water interface. In their investigation of the crossover of the hydrodynamics from 2D, interface-dominated behavior at high surface viscosities to bulk fluid dependent behavior at lower surface viscosities, the authors treated the particles explicitly as points.

We might expect this far-field approximation to break down when the inclusions are close together, a situation that is common, for example, in cellular membranes. However, in the 2D limit, when the inclusion pairs have small radii  $a < \ell_S$ , and the energy is primarily dissipated in the membrane [39], our experiments with small oil drops in 8CB films indicate that the mutual mobilities do not in fact depend on the inclusion size. Remarkably, even when the separation between the drops is comparable to or smaller than the Saffman length, the mutual mobilities  $M_{12}^{rr}$  and  $M_{12}^{\theta\theta}$  in this regime closely approximate the ‘parallel’  $\alpha_{\parallel}$  and ‘perpendicular’  $\alpha_{\perp}$  components of the LM response function tensor  $\alpha_{\alpha\beta}$  [16]. This result can be understood qualitatively by considering the flow induced by the motion of a single, isolated inclusion of small radius  $a/\ell_S < 1$  (see Fig. 3a). For small inclusions, the fore-aft vector field and the flow beside the inclusion are seen to fall off logarithmically in the vicinity of the inclusion, implying that a finite-sized second inclusion experiences the same mean flow as a point at the center of that inclusion when the two inclusions move radially or tangentially.

It is above the crossover from 2D to 3D hydrodynamics, with larger islands in the regime  $a > \ell_S$ , when the energy dissipation primarily occurs in the air surrounding the smectic film, that experiments performed with larger smectic islands show deviations of the mutual mobilities from the far-field solutions given by the LM response functions  $\alpha_{\parallel}$  and  $\alpha_{\perp}$ , as shown in Fig. 9. The deviation is particularly pronounced for the tangential mutual mobility  $M_{12}^{\theta\theta}$ , with the experimental values departing significantly from the far-field approximation  $\alpha_{\perp}$ , especially at shorter distances and for larger values of  $a/\ell_S$  (Fig. 9b). Since the  $M_{12}^{\theta\theta}$  is a much weaker (and harder to measure) quantity than  $M_{12}^{rr}$ , the experimental error bars in Fig. 9b are bigger. For larger  $a/\ell_S$  ratios, the flow due to the motion of a single, isolated inclusion decays faster (asymptotically as  $1/r$  and  $1/r^2$  in the fore-aft direction and in the regions beside the inclusion, respectively) than the flow field due to an inclusion of a small radius, as seen in (see Fig. 3b). In this case, the flow that a finite-sized second inclusion experiences can

no longer be approximated by the mean flow at the center of that inclusion but depends both on the radius of the inclusions and on their proximity.

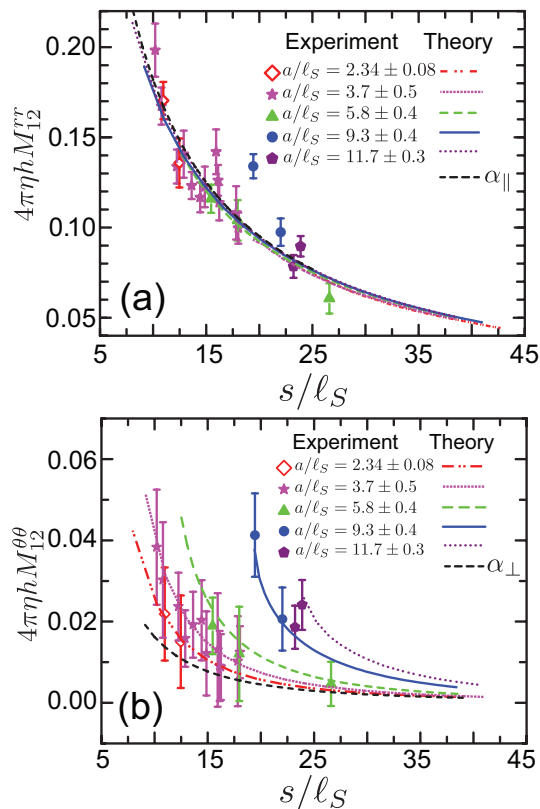


FIG. 9. Color online. Measured and calculated mutual mobilities (a)  $M_{12}^{rr}$  (radial) and (b)  $M_{12}^{\theta\theta}$  (tangential) as a function of dimensionless separation  $s/\ell_S$  for smectic islands of various sizes in the regime  $a > \ell_S$  [16].

It is interesting to note that the radial mutual mobility  $M_{12}^{rr}$  of a pair of circular inclusions of equal radius (Fig. 9a) is quite accurately described by the response function  $\alpha_{||}$  of Levine and MacKintosh for point-like particles even when the inclusions are close together. When inclusions have different radii, however, or do not have circular symmetry (for example, if they are elliptical), then our calculations show that the radial mutual mobility becomes size-dependent, and can no longer be approximated by  $\alpha_{||}$  of Levine and MacKintosh.

#### IV. MULTIPOLE EXPANSION OF THE FLUID VELOCITY FIELD

To explore further the effect of inclusion symmetry on radial mutual mobility, we considered the hydrodynamic interactions of pairs of clusters, each represented by a discrete arrangement of small blobs on the surface of the model membrane. We assume that these clusters move as rigid bodies with prescribed velocities. The fluid velocity

field due to the motion of such clusters is then modeled as a linear superposition of the velocity fields due to localized, point-like forces acting on the membrane at the blob centers. We avoid the logarithmic divergence of the response functions  $\alpha_{||}(z)$  and  $\alpha_{\perp}(z)$  in Eqs. (4) and (5) in the limit  $z \rightarrow 0$  by allowing the forces to be ‘smeared’ over the blobs and evaluating the fluid velocity at their rims. This approach is similar to that of the Kirkwood approximation used in [30, 40, 41] and the regularized Stokeslet method used in [17]. In the following section, we derive a multipole expansion of the fluid velocity field due to the motion of the rigid clusters and investigate the dependence of the leading order term in the expansion on the number and spatial arrangement of the blobs. Using this multipole expansion, we show that the contributions of the higher-order terms to the radial mutual mobility are small for any symmetric arrangement of the blobs but that this is not the case for the tangential mutual mobility. We now outline the calculation of the leading order term in the expansion.

BEM calculations with no-slip boundary conditions on both inclusion boundaries, outlined in Appendix D, show that the dependence of the radial mutual mobility  $M_{12}^{rr}$  of a particular class of moving, rigid clusters on the distance  $s$  between the cluster centers quickly converges to the LM response function  $\alpha_{||}(s)$ . The clusters that exhibit such behavior are collections of discrete points at the vertices of regular polygons that have  $2n$ -fold rotational symmetry (such as squares, hexagons, and octagons) and are oriented so that there is mirror symmetry about the  $x$ - and  $y$ - axes.

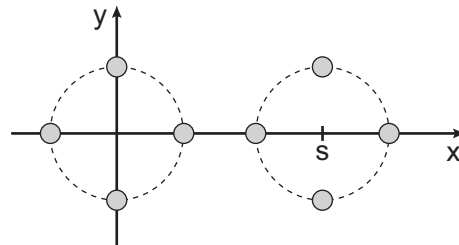


FIG. 10. Two discrete clusters, each comprising, in this example, four small blobs arranged on the vertices of a square oriented so that there is reflection symmetry in  $x$  and  $y$ . The mutual- and self-mobilities are computed by allowing the clusters to move along the  $x$ - and  $y$ -axes with velocity  $V$ , as in Fig. 7.

The fluid velocity field due to two discrete clusters generated at an arbitrary position  $\mathbf{x}$  in the two-dimensional membrane is given by

$$v_{\alpha}(\mathbf{x}) = \sum_{i=1}^2 \sum_{j=1}^N \alpha_{\alpha\beta}(\mathbf{x} - \mathbf{x}_j^{(i)}) f_{j,\beta}^{(i)}, \quad (21)$$

where the index  $i = 1, 2$  labels the cluster,  $j = 1, \dots, N$  labels the vertices in a cluster, and  $f_{j,\beta}^{(i)}$  are the point forces. We may expand the response tensor  $\alpha_{\alpha\beta}$  about the geometrical centers  $\mathbf{x}_c^{(i)}$  of the clusters, obtaining

$$\begin{aligned}
v_\alpha(\mathbf{x}) &= \sum_{i=1}^2 \sum_{j=1}^N \alpha_{\alpha\beta}(\mathbf{x} - \mathbf{x}_c^{(i)} + \mathbf{x}_c^{(i)} - \mathbf{x}_j^{(i)}) f_{j,\beta}^{(i)} \\
&= \sum_{i=1}^2 \alpha_{\alpha\beta}(\mathbf{x} - \mathbf{x}_c^{(i)}) \sum_{j=1}^N f_{j,\beta}^{(i)} + \\
&\quad \sum_{i=1}^2 \nabla_\gamma \alpha_{\alpha\beta}(\mathbf{x} - \mathbf{x}_c^{(i)}) \sum_{j=1}^N (\mathbf{x}_c^{(i)} - \mathbf{x}_j^{(i)})_\gamma f_{j,\beta}^{(i)} + \dots (22)
\end{aligned}$$

This expansion resembles the multipole expansion commonly used in 3D hydrodynamics [42]. The flow field may be approximated by the leading term in the expansion of Eq. (22) as

$$v_\alpha(\mathbf{x}) \approx \sum_{i=1}^2 \alpha_{\alpha\beta}(\mathbf{x} - \mathbf{x}_c^{(i)}) F_\beta^{(i)}, \quad (23)$$

where  $F_\beta^{(i)} = \sum_{j=1}^N f_{j,\beta}^{(i)}$  is the  $\beta$ -component of the net force on the  $i$ -th cluster.

Let us assume that each cluster moves as a rigid body with velocity  $\mathbf{V}$  in the  $x$ -direction. We may choose  $\mathbf{x}$  in Eq. (23) to be one of the vertices  $\mathbf{x}_j^{(1)}$  of the first cluster. We then sum over all vertices  $j$ :

$$\begin{aligned}
V &= \frac{1}{N} \sum_{i=1}^2 \sum_{j=1}^N \alpha_{xx}(\mathbf{x}_j^{(1)} - \mathbf{x}_c^{(i)}) F_x^{(i)} \\
&= \tilde{M}_{11}^{rr} F_x^{(1)} + \tilde{M}_{12}^{rr} F_x^{(2)}, \quad (24)
\end{aligned}$$

where

$$\tilde{M}_{11}^{rr} = \frac{1}{N} \sum_{j=1}^N \alpha_{xx}(\mathbf{x}_j^{(1)} - \mathbf{x}_c^{(1)}) \quad (25)$$

and

$$\tilde{M}_{12}^{rr} = \frac{1}{N} \sum_{j=1}^N \alpha_{xx}(\mathbf{x}_j^{(1)} - \mathbf{x}_c^{(2)}) \quad (26)$$

are the approximate expressions for the self- and mutual mobilities within the leading order of the 2D ‘multipole’ expansion. Similarly, if the clusters move instead along the  $y$ -axis, with velocities  $\mathbf{V} = V\hat{y}$ , we find approximately

$$\tilde{M}_{11}^{\theta\theta} = \frac{1}{N} \sum_{j=1}^N \alpha_{yy}(\mathbf{x}_j^{(1)} - \mathbf{x}_c^{(1)}) \quad (27)$$

$$\tilde{M}_{12}^{\theta\theta} = \frac{1}{N} \sum_{j=1}^N \alpha_{yy}(\mathbf{x}_j^{(1)} - \mathbf{x}_c^{(2)}). \quad (28)$$

The relative deviation of the radial mutual mobility computed within the first order of multipole expansion (Eq. (26)) from the BEM result assuming no-slip conditions on the inclusion boundaries (see Appendix D),  $\Delta M_{12}^{rr} = (M_{12}^{rr} - \tilde{M}_{12}^{rr})/M_{12}^{rr}$ , is plotted in Fig. 11a as a

function of the scaled distance  $s/\ell_S$  between the cluster centers for clusters with different numbers of vertices  $N$ . The difference is rather small (less than 5% for clusters with more than 20 points). However, the first-order approximation of the tangential mutual mobility (see Eq. (28)) deviates significantly from the BEM calculations, even when  $N$  is large. It is clear that in the tangential case, the higher order terms in the multipole expansion cannot be neglected.

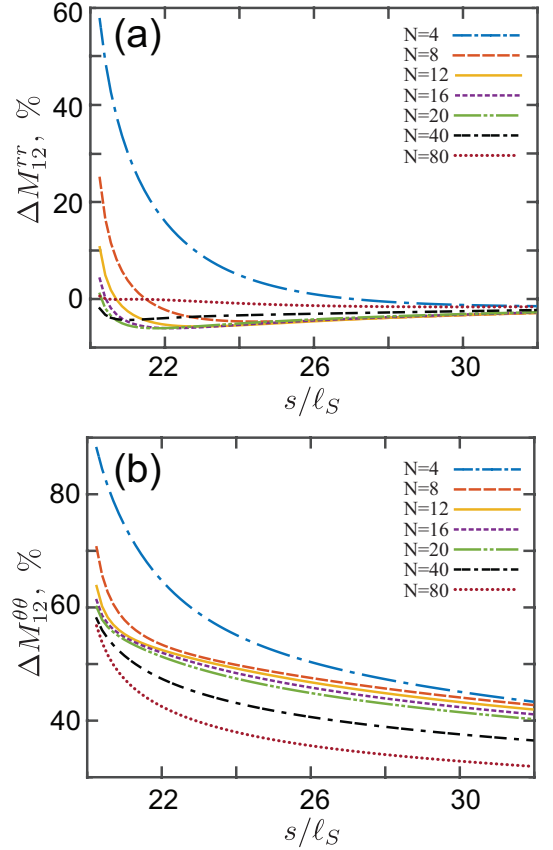


FIG. 11. Color online. Relative deviation of the approximate radial and angular mutual mobilities given by the leading term in the multipole expansion from the extended BEM calculations. The relative deviations (a)  $\Delta M_{12}^{rr}$  (b)  $\Delta M_{12}^{\theta\theta}$  are plotted vs. the dimensionless distance  $s/\ell_S$  between the cluster centers. The radii of the small blobs forming the clusters were set to  $\varepsilon = 0.01\ell_S$ . The vertices of the clusters lie on circles of radius  $a/\ell_S = 10$  at angular positions  $\phi_j = 2\pi(j-1)/N$ , with  $j = 1, \dots, N$ , where  $N$  is the number of blobs in each cluster and the angles  $\phi_j$  are measured from the  $x$ -axis.

When the inclusion does not have more than two-fold rotational symmetry, the radial mutual mobility becomes strongly size-dependent, and can no longer be approximated by the leading term in the multipole expansion. By way of example, the radial mutual mobilities of pairs of elliptical inclusions computed using the BEM method are plotted as a function of their dimensionless separation  $s/\ell_S$  in Fig. 12. The computed  $M_{12}^{rr}$  also deviates

from the LM response function  $\alpha_{\parallel}$  except when  $a = b$ , i.e., when the inclusions are circular, as shown in Fig. 12. Since we have no measurements of the mobilities of elliptical inclusions, we are unable to compare the theoretical predictions with experiment.

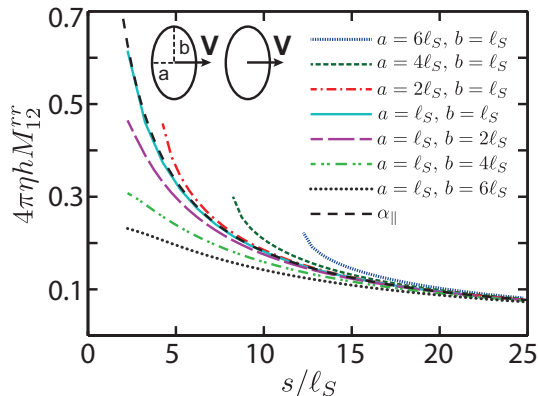


FIG. 12. Color online. Radial mutual mobility of two elliptical inclusions with different aspect ratios plotted against distance  $s$  between their centers scaled by the Saffman length. The black dashed curve is the LM response function  $\alpha_{\parallel}$ , describing well the case of two circular inclusions of radius  $\ell_S$ .

## V. CONCLUSION

We have probed experimentally and theoretically the hydrodynamic behavior of a circular inclusion in a thin fluid membrane in the vicinity of a linear boundary, and of a pair of inclusions near one another. We have developed a computational method that generalizes the point particle approach of Levine and MacKintosh [14] using a boundary-element technique in order to model inclusions of finite extent and arbitrary separation.

The agreement between our model predictions and experimental measurements of the mobilities of inclusions moving parallel and perpendicular to the film boundary (meniscus) is very good. We observe that the inclusion mobility is reduced by the presence of a boundary, as expected, and that the rate at which the mobility approaches the HPW mobility of a disk in an unbounded membrane as the distance from the boundary increases depends on the ratio of the inclusion radius to the Saffman length,  $a/\ell_S$ . This dependence on  $a/\ell_S$  reflects the crossover from 2D hydrodynamics ( $a/\ell_S < 1$ ) to 3D hydrodynamics ( $a/\ell_S > 1$ ), with, correspondingly, slower and faster decay rates of the flow fields. Quite surprisingly, a far-field approximation for the inclusion mobilities based on a simplified version of the method of reflections works rather well, even down to distances between the inclusion and the boundary of as little as two or three inclusion radii. The far-field approximation can confidently be used to compute flow fields and mobilities for both moderate and large separations between an

inclusion and the boundary and is much less computationally expensive than the expanded boundary-element calculations.

The boundary-element model gives estimates of the mutual mobilities of two inclusions that are in good agreement with experiment. We observe that when  $a > \ell_S$ , the radial mutual mobility of two identical circular inclusions is independent of their radius, a consequence of the rotational symmetry of the inclusions. The leading order multipole expansion gives a good approximation of the velocity field in the membrane in the radial case. When the inclusions lack circular symmetry, the model predicts the radial and tangential mutual mobilities to be dependent on both the distance between inclusions and on their shape. These latter predictions have not yet been tested experimentally.

The computational scheme described here can be readily extended to study the hydrodynamic interactions of inclusions of arbitrary shape and number, both mobile and immobile.

## ACKNOWLEDGMENTS

This work was supported by NSF CBET-1437195, NASA Grant NNX-13AQ81G, and by the Soft Materials Research Center under NSF MRSEC Grants DMR-0820579 and DMR-1420736. TK would like to thank the Research Corporation for Science Advancement for support through a Cottrell College Science Award.

## Appendix A: Island Near a Boundary

### 1. Far-field approximation

We assume a coordinate system with the origin in the center of the inclusion and the linear boundary at  $x = d$ . To apply the simplified method of reflections, we approximate the flow field due to the moving inclusion by the flow field due to a single force  $\mathbf{F}$  applied to the membrane at the inclusion center. The fluid velocity due to this force at the linear boundary is determined according to Eq. (2) as

$$v_F^\alpha(y) = F^\beta \alpha_{\alpha\beta}(|d\hat{x} + y\hat{y}|). \quad (\text{A1})$$

Since the linear boundary is stationary, a no-slip boundary condition requires the fluid velocity at the boundary to vanish. To ‘cancel’ the fluid field due to the inclusion, Eq. (A1), we introduce a continuous distribution of ‘image’ forces  $g^\beta(y)$  along the boundary. The force distribution  $g^\beta(y)$  is determined from the integral equation:

$$-v_F^\alpha(y) = \int_{-\infty}^{\infty} dy' g^\beta(y') \alpha_{\alpha\beta}(|y' - y|). \quad (\text{A2})$$

We solved equations (A2) numerically by discretizing the integrand, truncating along the linear boundary the lim-

its of integration,  $\int_{-\infty}^{\infty} \rightarrow \int_{-L}^L$ , and replacing the integral by a sum. We then obtain

$$-v_F^\alpha(y_i) = \Delta_y \sum_{\substack{j=1 \\ i \neq j}}^{N_y} g^\beta(y_j) \alpha_{\alpha\beta}(|y_j - y_i|) + \mathcal{J}^\alpha(y_i), \quad (\text{A3})$$

where  $N_y$  is the number of grid points,  $\Delta_y = 2L/N_y$  is the grid spacing along the linear boundary, and  $\mathcal{J}^\alpha(\phi_i)$  denotes the diagonal term ( $i = j$ ) in the sum. We typically choose the truncation parameter  $L$  to be between  $10d$  and  $20d$  and the number of grid points  $N_y$  between 300 and 500.

Special treatment was applied to the diagonal  $i = j$  element  $\mathcal{J}^\alpha(y_i)$  in the sum due to the logarithmic divergence of the functions  $\alpha_{\parallel}(z)$  and  $\alpha_{\perp}(z)$  for  $z \rightarrow 0$  (see Eqs. (3)-(5)): we expanded the functions  $\alpha_{\parallel}(z)$  and  $\alpha_{\perp}(z)$  about  $z = 0$  and performed integrations analytically over a small interval in the vicinity of  $z = 0$ .

To calculate the terms  $\mathcal{J}^\alpha(y_i)$  in Eq. (A3), we integrated over  $(-\Delta_y/2, \Delta_y/2)$  near  $z = 0$ :

$$\begin{aligned} \mathcal{J}^y(y_i) &= g^y(y_i) \int_{-\Delta_y/2}^{\Delta_y/2} \alpha_{\parallel}\left(\left|\frac{z}{\ell_S}\right|\right) dz \\ &= \frac{2g^y(y_i)}{4\pi\eta h} \lim_{\varepsilon \rightarrow 0} \int_{\varepsilon}^{\Delta_y/2} \left[ \frac{1}{2} - \gamma + \frac{2z}{3\ell_S} + \log \frac{2\ell_S}{z} \right] dz \\ &= \frac{g^y(y_i)}{4\pi\eta h} \Delta_y \left[ \frac{3}{2} + \frac{\Delta_y}{6\ell_S} - \gamma + \log \left( \frac{4\ell_S}{\Delta_y} \right) \right]. \quad (\text{A4}) \end{aligned}$$

Here  $\gamma$  is the Euler constant. Similarly,

$$\begin{aligned} \mathcal{J}^x(y_i) &= g^x(y_i) \int_{-\Delta_y/2}^{\Delta_y/2} \alpha_{\perp}\left(\left|\frac{z}{\ell_S}\right|\right) dz \\ &= \frac{g^x(y_i)}{4\pi\eta h} \Delta_y \left[ \frac{1}{2} + \frac{\Delta_y}{3\ell_S} - \frac{\gamma}{6} + \log \left( \frac{4\ell_S}{\Delta_y} \right) \right]. \quad (\text{A5}) \end{aligned}$$

We solved the linear algebraic equations (A3) in MatLab.

The ‘reflected’ velocity field at the inclusion center due to the forces  $g^\beta(y)$  on the boundary is calculated as

$$v_r^\alpha(0) = \Delta_y \sum_{j=1}^{N_y} g^\beta(y_j) \alpha_{\alpha\beta}(|d\hat{x} + y_j\hat{y}|) \quad (\text{A6})$$

For an island moving perpendicular (parallel) to the boundary we set  $\mathbf{F} = 1 \cdot \hat{x}$  ( $\mathbf{F} = 1 \cdot \hat{y}$ ) in Eq. (A1). Therefore, the parameter  $\gamma(d)$  in Eq. (11) is equal to  $v_r^\alpha(0)$  in Eq. (A6) for motion perpendicular (parallel) to the boundary.

## 2. Boundary-Element Method

Let us assume that an island moves with translational velocity  $\mathbf{V}$  and rotates with angular velocity  $\mathbf{\Omega}$  about its geometric center. Therefore, each point on the island circumference has the total velocity

$$\mathbf{v}(\phi) = \mathbf{V} + \mathbf{\Omega} \times \mathbf{r}(\phi), \quad (\text{A7})$$

with  $\mathbf{r}(\phi) = a \cos \phi \hat{x} + a \sin \phi \hat{y}$ .

As follows from Eq. (12) and the no-slip boundary conditions, the fluid velocity at an azimuth  $\phi$  on the island circumference is given by

$$\begin{aligned} v^\alpha(\phi) &= \int_0^{2\pi} d\phi' f^\beta(\phi') \alpha_{\alpha\beta}(|\boldsymbol{\chi}(\phi, \phi')|) \\ &\quad + \int_{-\infty}^{\infty} dy' g^\beta(y') \alpha_{\alpha\beta}(|\boldsymbol{\xi}(\phi, y')|), \quad (\text{A8}) \end{aligned}$$

where  $v^\alpha(\phi)$  is given by Eq. (A7),  $\boldsymbol{\chi}(\phi, \phi') = a(\cos \phi - \cos \phi')\hat{x} + a(\sin \phi - \sin \phi')\hat{y}$ ,  $\boldsymbol{\xi}(\phi, y') = (a \cos \phi - d)\hat{x} + (a \sin \phi - y')\hat{y}$ . Similarly, the fluid velocity at the linear boundary is equal to zero and is related to the localized forces  $f^\beta(\phi)$  and  $g^\beta(y')$  via

$$\begin{aligned} v^\alpha(y) = 0 &= \int_0^{2\pi} d\phi' f^\beta(\phi') \alpha_{\alpha\beta}(|\boldsymbol{\zeta}(\phi', y)|) \\ &\quad + \int_{-\infty}^{\infty} dy' g^\beta(y') \alpha_{\alpha\beta}(|\boldsymbol{\eta}(y, y')|), \quad (\text{A9}) \end{aligned}$$

where  $\boldsymbol{\zeta}(\phi', y) = (a \cos \phi' - d)\hat{x} + (a \sin \phi' - y)\hat{y}$ ,  $\boldsymbol{\eta}(y, y') = (y' - y)\hat{y}$ .

We solved Eqs. (A8) and (A9) for  $f^\beta(\phi')$  and  $g^\beta(y')$  numerically by replacing the integrals by sums. Thus, for Eq. (A8) we obtain:

$$\begin{aligned} v^\alpha(\phi_i) &= \Delta_\phi \sum_{\substack{j=1 \\ i \neq j}}^{N_\phi} f^\beta(\phi'_j) \alpha_{\alpha\beta}(|\boldsymbol{\chi}(\phi_i, \phi'_j)|) \\ &\quad + \mathcal{I}^\alpha(\phi_i) \\ &\quad + \Delta_y \sum_{j=1}^{N_y} g^\beta(y_j) \alpha_{\alpha\beta}(|\boldsymbol{\xi}(\phi_i, y_j)|). \quad (\text{A10}) \end{aligned}$$

Here  $\Delta_\phi = 2\pi/N_\phi$  and  $\Delta_y = 2L/N_y$  are the grid spacings along the circumference and on the linear boundary respectively, and  $\mathcal{I}^\alpha(\phi_i)$  denotes the diagonal term ( $i = j$ ) in the first sum. As in the far-field computations, we typically choose the truncation parameter  $L$  to be between  $10d$  and  $20d$  and the number of grid points  $N_\phi, N_y$  between 300 and 500.

A similar discretization was performed for Eq. (A9):

$$\begin{aligned} 0 &= \Delta_\phi \sum_{j=1}^{N_\phi} f^\beta(\phi_j) \alpha_{\alpha\beta}(|\boldsymbol{\zeta}(y_i, \phi_j)|) \\ &\quad + \Delta_y \sum_{\substack{j=1 \\ i \neq j}}^{N_y} g^\beta(y_j) \alpha_{\alpha\beta}(|\boldsymbol{\eta}(y_i, y_j)|) \\ &\quad + \mathcal{J}^\alpha(y_i), \quad (\text{A11}) \end{aligned}$$

where  $\mathcal{J}^\alpha(y_i)$  stands for the diagonal term ( $i = j$ ) in the second sum.

To calculate the term  $\mathcal{I}^\alpha(\phi_i)$  in Eq. (A10), we integrated over a small arc length  $(-a\Delta_\phi/2, a\Delta_\phi/2)$  near

$z = 0$ , where  $a$  is the radius of the inclusion:

$$\begin{aligned} \mathcal{I}^x(\phi_i) &= f^x(\phi_i) \int_{-a\Delta_\phi/2}^{a\Delta_\phi/2} \alpha_{\parallel} \left( \left| \frac{z}{\ell_S} \right| \right) \frac{dz}{a} \\ &= \frac{2f^x(\phi_i)}{4\pi\eta h} \lim_{\varepsilon \rightarrow 0} \int_{\varepsilon}^{a\Delta_\phi/2} \left[ \frac{1}{2} - \gamma + \frac{2z}{3\ell_S} + \log \frac{2\ell_S}{z} \right] \frac{dz}{a} \\ &= \frac{f^x(\phi_i)}{4\pi\eta h} \Delta_\phi \left[ \frac{3}{2} + \frac{a\Delta_\phi}{6\ell_S} - \gamma + \log \left( \frac{4\ell_S}{a\Delta_\phi} \right) \right]. \quad (\text{A12}) \end{aligned}$$

Similarly,

$$\begin{aligned} \mathcal{I}^y(\phi_i) &= f^y(\phi_i) \int_{-a\Delta_\phi/2}^{a\Delta_\phi/2} \alpha_{\perp} \left( \left| \frac{z}{\ell_S} \right| \right) \frac{dz}{a} \\ &= \frac{2f^y(\phi_i)}{4\pi\eta h} \lim_{\varepsilon \rightarrow 0} \int_{\varepsilon}^{a\Delta_\phi/2} \left[ -\frac{1}{2} - \gamma + \frac{4z}{3\ell_S} + \log \frac{2\ell_S}{z} \right] \frac{dz}{a} \\ &= \frac{f^y(\phi_i)}{4\pi\eta h} \Delta_\phi \left[ \frac{1}{2} + \frac{a\Delta_\phi}{3\ell_S} - \frac{\gamma}{6} + \log \left( \frac{4\ell_S}{a\Delta_\phi} \right) \right]. \quad (\text{A13}) \end{aligned}$$

The terms  $\mathcal{J}^\alpha(y_i)$  in Eq. (A11) were calculated according to Eqs. (A4) and (A5).

In general, the integral equations (A8) and (A9) were reduced to a large system of linear algebraic equations that we solved simultaneously in MatLab.

The translational and rotational motions of the island are coupled in the proximity of a boundary. The viscous drag force  $\mathbf{F}$  and torque  $\mathbf{T}$  on the island are linear functions of its translational and rotational velocities:

$$\begin{pmatrix} \mathbf{F} \\ \mathbf{T} \end{pmatrix} = \boldsymbol{\zeta} \begin{pmatrix} \mathbf{V} \\ \boldsymbol{\Omega} \end{pmatrix}, \quad (\text{A14})$$

where  $\boldsymbol{\zeta}$  is the resistance matrix. Rewriting this equation in components we arrive at

$$\begin{pmatrix} F^x \\ F^y \\ T \end{pmatrix} = \begin{pmatrix} \zeta_{\perp} & 0 & 0 \\ 0 & \zeta_{\parallel} & \zeta_{\parallel,R} \\ 0 & \zeta_{\parallel,R} & \zeta_R \end{pmatrix} \begin{pmatrix} V^x \\ V^y \\ \Omega \end{pmatrix}, \quad (\text{A15})$$

The resistance matrix was calculated numerically. For example, to find the third column of the resistance matrix, we set  $V^x = V^y = 0$  and  $\Omega \neq 0$  and solved the system of equations (A10) and (A11) for the force densities  $f^\alpha(\phi_i)$  and  $g^\alpha(y)$ . The net force and the torque on the island are calculated as  $F^\alpha = \Delta_\phi \sum_{i=1}^{N_\phi} f^\alpha(\phi_i)$  and  $T = a\Delta_\phi \sum_{i=1}^{N_\phi} (\cos \phi_i f^y(\phi_i) - \sin \phi_i f^x(\phi_i))$ , respectively. The force-torque vector determines the third column of the resistance matrix.

The mobility matrix  $\mathbf{M}$  is the inverse of the resistance matrix:

$$\mathbf{M} = \boldsymbol{\zeta}^{-1} = \begin{pmatrix} \mu_{\perp} & 0 & 0 \\ 0 & \mu_{\parallel} & \mu_{\parallel,R} \\ 0 & \mu_{\parallel,R} & \mu_R \end{pmatrix} \quad (\text{A16})$$

Our computations predict very weak coupling of translational and rotational motions for islands of experimentally relevant radii ( $0.1\ell_S < a < 10\ell_S$ ), with off-diagonal coupling terms  $\mu_{\parallel,R}$  being at least two orders

of magnitude smaller than the diagonal terms in the mobility matrix. We, therefore, neglected the rotational-translational coupling and followed the simplified computational scheme described in the main text.

## Appendix B: Hydrodynamic Interactions of Two Circular Inclusions

The origin of the coordinate system is chosen in this case to be the center of the circular inclusion with index ‘1’. The center of inclusion ‘2’ is at  $s\hat{x}$ . The inclusions are assumed to have equal radii  $a$ . From Eq. (19), the fluid velocity at azimuth  $\phi$  on the circumference of inclusion ‘1’ is given by

$$\begin{aligned} v_1^\alpha(\phi) = V_1^\alpha &= \int_0^{2\phi} d\phi' f_1^\beta(\phi') \alpha_{\alpha\beta}(|\mathbf{u}(\phi, \phi')|) \\ &+ \int_0^{2\phi} d\phi' f_2^\beta(\phi') \alpha_{\alpha\beta}(|\mathbf{z}(\phi, \phi')|), \quad (\text{B1}) \end{aligned}$$

where  $\mathbf{u}(\phi, \phi') = a(\cos \phi - \cos \phi')\hat{x} + a(\sin \phi - \sin \phi')\hat{y}$  and  $\mathbf{z}(\phi, \phi') = (a \cos \phi - s - a \cos \phi')\hat{x} + a(\sin \phi - \sin \phi')\hat{y}$ .

Similarly, for the fluid velocity at a point on the boundary of the second inclusion we have

$$\begin{aligned} v_2^\alpha(\phi) = V_2^\alpha &= \int_0^{2\phi} d\phi' f_1^\beta(\phi') \alpha_{\alpha\beta}(|\mathbf{u}'(\phi, \phi')|) \\ &+ \int_0^{2\phi} d\phi' f_2^\beta(\phi') \alpha_{\alpha\beta}(|\mathbf{z}'(\phi, \phi')|), \quad (\text{B2}) \end{aligned}$$

where  $\mathbf{u}'(\phi, \phi') = (a \cos \phi - s - a \cos \phi')\hat{x} + a(\sin \phi - \sin \phi')\hat{y}$  and  $\mathbf{z}'(\phi, \phi') = a(\cos \phi - \cos \phi')\hat{x} + a(\sin \phi - \sin \phi')\hat{y}$ .

Using the same approach as in Appendix A, we may solve Eqs. (B1) and (B2) for  $f_1^\beta(\phi)$  and  $f_2^\beta(\phi)$  numerically by discretizing the integrands and replacing the integrals by sums. For example, for Eq. (B1) we arrive at

$$\begin{aligned} V_1^\alpha(\phi_i) &= \Delta_\phi \sum_{\substack{j=0 \\ i \neq j}}^{N_\phi} f_1^\beta(\phi'_j) \alpha_{\alpha\beta}(|\mathbf{u}(\phi_i, \phi'_j)|) \\ &+ \mathcal{I}^\alpha(\phi_i) \\ &+ \Delta_\phi \sum_{j=0}^{N_\phi} f_2^\beta(\phi'_j) \alpha_{\alpha\beta}(|\mathbf{z}(\phi_i, \phi'_j)|), \quad (\text{B3}) \end{aligned}$$

where  $N_\phi$  is the number of grid points on the boundary,  $\Delta_\phi = 2\pi/N_\phi$  is the grid spacing, and  $\mathcal{I}^\alpha(\phi_i)$  denotes the diagonal element ( $i = j$ ) in the first sum. The logarithmic divergence in these terms is dealt with in the same manner described in Appendix A.

The integral equations (B1), (B2) were thus reduced to a large system of linear algebraic equations that we solved numerically in MatLab.

### Appendix C: Generalized Stokes-Einstein Relations

The cross-correlation function of particle velocities  $V_i^\alpha$  is related to their mutual mobilities by the generalized fluctuation-dissipation theorem [43]:

$$\langle V_i^\alpha(0) \tilde{V}_j^\beta(p) \rangle = k_B T (\tilde{M}_{ij}(p))^{\alpha\beta}. \quad (\text{C1})$$

Here  $i, j$  are particle indices ( $i, j = 1, 2$ ),  $\alpha, \beta = r, \theta$  represent the radial and angular coordinates, and  $\mathbf{M}_{ij}^{\alpha\beta}$  are the self- and mutual mobilities of the particles. The tilde ( $\tilde{\phantom{x}}$ ) denotes the Laplace transform:

$$\tilde{F}(p) \equiv \mathcal{L}(F(t)) = \int_0^\infty e^{-pt} F(t) dt. \quad (\text{C2})$$

In the experiments, we measure the inclusion displacements rather than their velocities and, therefore, turn to the cross-correlation function for the particle displacements  $\langle \Delta r_i^\alpha(t) \Delta r_j^\beta(t) \rangle$ , where  $\Delta \mathbf{r}(t) = \mathbf{r}(t) - \mathbf{r}(0)$ . The particle displacement correlation function is related to the velocity correlation function by [44]

$$\langle \Delta r_i^\alpha(t) \Delta r_j^\beta(t) \rangle = 2 \int_0^t dt' \langle V_i^\alpha(0) V_j^\beta(t') \rangle (t - t'). \quad (\text{C3})$$

The Laplace transform of the displacement correlation function is

$$\begin{aligned} \mathcal{L}(\langle \Delta r_i^\alpha(t) \Delta r_j^\beta(t) \rangle) &= 2 \langle V_i^\alpha(0) \mathcal{L} \left( \int_0^t dt' V_j^\beta(t') (t - t') \right) \rangle \\ &= \frac{2}{p^2} \langle V_i^\alpha(0) \tilde{V}_j^\beta(p) \rangle, \end{aligned} \quad (\text{C4})$$

where we first interchanged the order of ensemble averaging and the Laplace transform and then used the convolution theorem. From Eqs. (C1) and (C4) we have

$$\mathcal{L}(\langle \Delta r_i^\alpha(t) \Delta r_j^\beta(t) \rangle) = \frac{2k_B T (\tilde{M}_{ij}(p))^{\alpha\beta}}{p^2}, \quad (\text{C5})$$

where  $\tilde{M}_{ij}^{\alpha\beta}(p)$  is the Laplace transform of  $M_{ij}^{\alpha\beta}(t - t')$ . Assuming that the smectic film is a simple viscous fluid, we have  $M_{ij}^{\alpha\beta}(t - t') = M_{ij}^{\alpha\beta} \delta(t - t')$ .

Performing the inverse Laplace transform of Eq. (C5), we obtain

$$\langle \Delta r_i^\alpha(t) \Delta r_j^\beta(t) \rangle = 2k_B T (M_{ij})^{\alpha\beta} t \quad (\text{C6})$$

Since the islands have mirror symmetry about the line connecting their centers,  $(M_{ij})^{\alpha\beta} = 0$  for  $\alpha \neq \beta$ . In

particular, the cross-correlation function for two islands with their centers separated by a distance  $s$  is:

$$\begin{aligned} \langle \Delta \mathbf{r}_1(t) \cdot \Delta \mathbf{r}_2(t) \delta(r_{12}(0) - s) \rangle &= \\ &= 2k_B T (M_{12}^{rr}(s) + M_{12}^{\theta\theta}(s)) t. \end{aligned} \quad (\text{C7})$$

Here  $\Delta \mathbf{r}_1(t)$  and  $\Delta \mathbf{r}_2(t)$  refer to displacements of islands 1 and 2 respectively in time interval  $t$ .

### Appendix D: Hydrodynamic Interactions of Two Clusters

In the discrete approximation, each cluster comprises an even number of small disks (blobs) of radius  $\varepsilon$ . Each such cluster moves as a rigid body with prescribed velocity  $\mathbf{V}$ . The origin of the coordinate system is placed at the geometric center of the cluster with index ‘1’. The center of the second cluster is at position  $s\hat{x}$ . The fluid velocity at the  $i$ -th vertex of the cluster with index ‘1’ is given by

$$\begin{aligned} V_\alpha &= \sum_{\substack{j=1 \\ i \neq j}}^N \alpha_{\alpha\beta} (\mathbf{x}_i^{(1)} - \mathbf{x}_j^{(1)}) f_{j,\beta}^{(1)} + \alpha_{\alpha\beta}(\varepsilon) f_{i,\beta}^{(1)} \\ &+ \sum_{j=1}^N \alpha_{\alpha\beta} (\mathbf{x}_i^{(1)} - \mathbf{x}_j^{(2)}) f_{j,\beta}^{(2)}, \end{aligned} \quad (\text{D1})$$

where  $\alpha, \beta = x, y$ ;  $j = 1, \dots, N$  labels the vertices in the cluster,  $\mathbf{x}_j^{(i)}$  is the position of  $j$ -th vertex (blob) in the  $i$ -th cluster, and  $f_{j,\beta}^{(i)}$  are the point forces. To avoid the logarithmic singularity in  $\alpha_{\alpha\beta}(z)$  as  $z \rightarrow 0$ , the diagonal term in the first sum is evaluated at the rim of each blob.

A similar expression can be written for the flow field at the  $i$ -th vertex of the cluster with index ‘2’:

$$\begin{aligned} V_\alpha &= \sum_{\substack{j=1 \\ i \neq j}}^N \alpha_{\alpha\beta} (\mathbf{x}_i^{(2)} - \mathbf{x}_j^{(2)}) f_{j,\beta}^{(1)} + \alpha_{\alpha\beta}(\varepsilon) f_{i,\beta}^{(2)} \\ &+ \sum_{j=1}^N \alpha_{\alpha\beta} (\mathbf{x}_i^{(2)} - \mathbf{x}_j^{(1)}) f_{j,\beta}^{(1)}. \end{aligned} \quad (\text{D2})$$

By imposing no-slip boundary conditions on the vertices of the clusters (i. e. on the blobs), from Eqs. (D1) and (D2) we arrive at a set of  $2N$  algebraic equations that we solved in MatLab. In our computations we gradually reduce the magnitude of the parameter  $\varepsilon$ , the size of the blobs at the vertices of the clusters, until the solution converges, showing changes smaller than 1% with further reduction of the parameter  $\varepsilon$ .

[1] N. Oppenheimer and H. Diamant, Biophys. J. **96**, 3041 (2009).

[2] P. G. Saffman and M. Delbrück, Proc. Natl. Acad. Sci.

USA **72**, 3111 (1975).

[3] P. G. Saffman, J. Fluid Mech. **73**, 593 (1976).

[4] B. D. Hughes, B. A. Pailthorpe, and L. R. White,

- J. Fluid Mech. **110**, 349 (1981).
- [5] N. Oppenheimer and H. Diamant, Phys. Rev. Lett. **107**, 258102 (2011).
- [6] J. R. Heringa, F. W. Wiegel, and F. P. H. van Beckum, Physica **108A**, 598 (1981).
- [7] F. W. Wiegel and J. R. Heringa, Can. J. Phys. **63**, 44 (1985).
- [8] E. Petrov and P. Schwille, Biophys. J. **94**, L41 (2008).
- [9] P. Cicuta, S. L. Keller, and S. L. Veatch, J. Phys. Chem. B Lett. **111**, 3328 (2007).
- [10] C. Cheung, Y. H. Hwang, X.-l. Wu, and H. J. Choi, Phys. Rev. Lett. **76**, 2531 (1996).
- [11] E. P. Petrov, R. Petrosyan, and P. Schwille, Soft Matter **8**, 7552 (2012).
- [12] Z. H. Nguyen, M. Atkinson, C. S. Park, J. MacLennan, M. Glaser, and N. Clark, Phys. Rev. Lett. **105**, 268304 (2010).
- [13] S. J. Bussell, D. L. Koch, and D. A. Hammer, J. Fluid Mech. **243**, 679 (1992).
- [14] A. J. Levine and F. C. MacKintosh, Phys. Rev. E **66**, 061606 (2002).
- [15] M. Abramowitz and I. Stegun, *Handbook of Mathematical Functions* (Dover Publications, 1965).
- [16] Z. Qi, Z. H. Nguyen, C. S. Park, M. A. Glaser, J. E. MacLennan, N. A. Clark, T. Kuriabova, and T. R. Powers, Phys. Rev. Lett. **113**, 128304 (2014).
- [17] E. Noruzifar, B. A. Camley, and F. L. H. Brown, J. Chem. Phys. **141**, 124711 (2014).
- [18] C. Y. Young, R. Pindak, N. A. Clark, and R. B. Meyer, Phys. Rev. Lett. **40**, 773 (1978).
- [19] C. D. Muzny and N. A. Clark, Phys. Rev. Lett. **68**, 804 (1992).
- [20] J. C. Geminard, R. Holyst, and P. Oswald, Phys. Rev. Lett. **78**, 1924 (1997).
- [21] A. Eremin, S. Baumgarten, K. Harth, R. Stannarius, Z. H. Nguyen, A. Goldfain, C. S. Park, J. E. MacLennan, M. A. Glaser, and N. A. Clark, Phys. Rev. Lett. **107**, 268301 (2011).
- [22] H. Faxen, Ark. Mat., Astron. Fys. **17**, 1 (1923).
- [23] H. Brenner, Chem. Eng. Sci. **16**, 242 (1961).
- [24] A. J. Goldman, R. G. Cox, and H. Brenner, Chem. Eng. Sci. **22**, 637 (1967).
- [25] A. J. Leadbetter, J. L. A. Durrant, and M. Rugman, Molecular Crystals and Liquid Crystals **34**, 231 (1976).
- [26] F. Schneider, Phys. Rev. E **74**, 021709 (2006).
- [27] R. C. Weast, *Handbook of Chemistry and Physics*, 54th ed. (CRC Press, Cleveland, 1973-1974).
- [28] D. Davidov, C. R. Safinya, M. Kaplan, S. S. Dana, R. Schaetzling, R. J. Birgeneau, and J. D. Litster, Phys. Rev. B **19**, 1657 (1979).
- [29] J. Happel and H. Brenner, *Low Reynolds number hydrodynamics: with special applications to particulate media*, Mechanics of Fluids and Transport Processes Series (Martinus Nijhoff, 1965).
- [30] A. J. Levine, T. B. Liverpool, and F. C. MacKintosh, Phys. Rev. E **69**, 021503 (2004).
- [31] F. Picano, R. Holyst, and P. Oswald, Phys. Rev. E **62**, 3747 (2000).
- [32] P. Oswald and P. Pieranski, *Smectic and Columnar Liquid Crystals* (CRC Press, Boca Raton, 2006).
- [33] B. A. Camley and L. H. Brown, Soft Matter **9**, 4767 (2013).
- [34] J. Canny, "IEEE transactions on pattern analysis and machine intelligence," (IEEE, 1986) pp. 679-698.
- [35] G. Taubin, "IEEE transactions on pattern analysis and machine intelligence," (IEEE, 1991) pp. 1115-1138.
- [36] Z. Qi, C. S. Park, M. A. Glaser, J. E. MacLennan, and N. A. Clark, Phys. Rev. E **93**, 012706 (2016).
- [37] H. Schüring and R. Stannarius, Langmuir **18**, 9735 (2002).
- [38] V. Prasad, S. A. Koehler, and E. R. Weeks, Phys. Rev. Lett. **97**, 176001 (2006).
- [39] H. A. Stone, J. Fluid Mech. **645**, 1 (2010).
- [40] V. Bloomfield, W. Dalton, and K. V. Holde, Biopolymers **5**, 135 (1967).
- [41] M. Doi and S. F. Edwards, *The Theory of Polymer Dynamics* (Clarendon Press, 1988).
- [42] S. Kim and J. S. Karrila, *Microhydrodynamics: Principles and Selected Applications*. (Butterworth-Heinemann, Boston, MA, 1991).
- [43] T. M. Squires and T. G. Mason, Annu. Rev. Fluid Mech. **42**, 413 (2010).
- [44] F. Reif, *Fundamentals of Statistical and Thermal Physics* (Waveland Press, 1965).